Nonresonant multiphoton ionization of cesium in strong fields: Angular distributions and above-threshold ionization

G. Petite, F. Fabre, and P. Agostini
Centre d'Etudes Nucléaires de Saclay, Service de Physique des Atomes et des Surfaces, Commissariat à l'Energie Atomique, F-91191 Gif-sur-Yvette Cedex, France

M. Crance and M. Aymar
Laboratoire Aimé Cotton, Centre National de la Recherche Scientifique II, Bâtiment 505, Campus d'Orsay, F-91405 Orsay, France

(Received 21 October 1983)

Multiphoton ionization of cesium atoms by intense (5×10^{11} W cm^{-2}), short (54 ps) laser pulses at the neodymium-doped yttrium aluminum garnet laser frequency is studied. Experimentally, the energy spectrum and angular distribution of the photoelectrons are recorded using a time-of-flight spectrometer. Strong-field effects are clearly demonstrated by evidence of simultaneous four- and five-photon ionization (above-threshold ionization) and by intensity-dependent angular distributions. Theoretically, differential generalized cross sections for four- and five-photon ionization are computed and are shown to be strongly affected by light shifts and high-order coupling of nonresonant bound states. Comparison between theory and experiment includes effective order of nonlinearity, intensity dependence of four- and five-photon electron signal around the saturation intensity, relative values of angular-distribution coefficients, and the ratio of five- to four-photon signals. Intensity effects are generally well predicted both for angular distributions and for saturation. Some discrepancy remains between experimental and theoretical angular-distribution coefficients. The ratio of the total number of electrons emitted in the five- and four-photon processes is measured to be $(2.9\pm0.5)\times10^{-2}$, at 6×10^{11} W cm^{-2}, encompassing the theoretical value of 3.3×10^{-2}.

I. INTRODUCTION

Since high-powered lasers have been available, there has been a constant interest in the study of atoms interacting with intense light fields. As pointed out early by Bunkin and Prokhorov,[1] when light intensity is increased, multiphoton ionization (MPI)[2] becomes the dominant process. For laser intensities as high as 10^{15} W cm^{-2}, 22 MPI of He was observed. Experimental orders of nonlinearity were measured and found equal to the number of photons absorbed in the process. This supported the idea that, except in some special circumstances (resonant processes, for instance) lowest-order perturbation theory (LOPT) was sufficient to describe MPI processes. However, there has been several indications in the recent past that this is not the case. First, precise measurements of absolute MPI cross sections were made[2-4] and it was shown[5,6] that high-order corrections had to be introduced in the calculation of MPI cross sections to satisfactorily account for the measured values. On the other hand, study of the energy spectrum of the outgoing electrons showed the existence of above-threshold ionization (ATI).[7-11] In ATI processes an atom which could ionize by absorption of only N photons absorbs $(N+1)$, $(N+2)$, ..., or $(N+S)$ photons releasing an electron with an extra kinetic energy of 1, 2, ..., or S times the photon energy. These ATI processes coexist with any MPI process and whether they give rise to significant contributions or not is mainly a matter of laser intensity. An important result of Ref. 11 is that in the case of high intensities ($\simeq10^{13}$ W cm^{-2}) the probability of all $(N+S)$-order ATI processes (in this case $N=11$, $S=1-7$) behaves as I^K, with $K\simeq N$. This is a decisive argument against the idea that the observation of an N-power-law intensity dependence of the MPI ion yield proves that LOPT can be used to describe such processes. The results of Ref. 11 definitely call for a nonperturbative treatment of MPI.

For experimental convenience, all ATI experiments thus far have used xenon, a choice particularly inappropriate for comparison with theory. There is a need for an ATI experiment whose results could be compared with theoretical predictions. Most of the calculations concerning ATI have been done for hydrogen[12-14] with one exception[15] dealing with cesium and potassium. Cesium is a good candidate because it can be rather easily handled in an experiment and has already been successfully used for such a comparison. However, since it ionizes rather easily, compared to Xe or H, high-intensity effects can only be observed using ultrashort laser pulses.[15]

Besides the ATI problem, recently there has been an upsurge of interest concerning the question of the angular distribution of the photoelectrons, leading to both experimental[16-21] and theoretical[22,23] works. Most of them[16-19,22] deal with resonant processes whose interpretation is simpler since some of the multiphoton aspect of the problem is removed by the resonant character of the ionization process. However, if the resonant state has an unresolved fine-structure splitting, the Stark shifts of the

two components were shown to change the interference conditions between the two ionization channels, and an intensity dependence of the angular distribution was observed.[22]

Here again, the issue of higher-order corrections to LOPT is addressed. Recently angular distributions were recorded in the case of the five-photon ionization of sodium at 1.06 μm (Ref. 21) (nonresonant, unfortunately without energy analysis) and calculations of the same were made in Ref. 23 but the result of the comparison is rather unsatisfactory.

In this paper we present both an experimental and a theoretical study of the four-photon ionization of cesium at the Nd:Yag laser frequency. The intensity range considered is 10^9–10^{12} W cm^{-2}, where high-intensity effects are expected to be significant. The emphasis is put on the two points discussed above: the angular distribution and ATI.

In Sec. II, we present the calculations of differential and total cross sections for four- and five-photon ionization of cesium at the Nd:Yag frequency. Section III describes the experimental setup. In Sec. IV, we present the angular-distribution measurements and discuss how they compare to our theoretical results. Above-threshold ionization measurements are presented and discussed in Sec. V.

II. CALCULATION OF FOUR-AND FIVE-PHOTON IONIZATION CROSS SECTIONS

Various methods have been developed to calculate above-threshold ionization cross sections which are essentially based on perturbation theory at minimum nonvanishing order. Such a treatment is valid in the low-field limit and is generally considered as correct for nonresonant situations, that is, when the field frequency and its harmonics are far enough from any atomic Bohr frequency. However, in a previous study of four-photon ionization in the range 9200–9600 cm^{-1} (Ref. 24), it has been shown that resonance effects have to be taken into account even at nonresonant frequencies, when the field intensity becomes as large as 10^{10} W cm^{-2}. For nonresonant situations, we proposed a method to calculate the dynamics of above-threshold ionization.[15,25] Here this method is generalized to resonant processes.

A. Principle of the calculation

In the dressed-atom picture, the Hamiltonian is

$$H = H_{\rm at} + H_f + V \,, \tag{1}$$

where $H_{\rm at}$ is the atomic Hamiltonian and H_f is the free-field Hamiltonian. The interaction Hamiltonian is

$$V = rC_0^{(1)}(a + a^\dagger) \,, \tag{2}$$

where $rC_0^{(1)}$ is the dipole operator for linearly polarized light; a and $a^\dagger$ are the annihilation and creation operators for the ω mode. Initially, the atom is in state $|0\rangle$ with energy E_0. Ionization occurs to atomic continuum states $|E_\alpha^{\vec{k}}\rangle$ with energy E^k such that $(E^k - E_0)/\hbar\omega$ is close to a positive integer q_k ($\hbar\vec{k}$ is the electron momentum, α labels the continua with the same energy but different quantum numbers). Quasiresonant states are discrete atomic states $|i\rangle$, with energy E_i such that $(E_i - E_0)/\hbar\omega$ is close to an integer q_i. When the atom is irradiated by a light flux $N_0\hbar\omega c$, ionization results from the interaction of the nearly degenerate dressed-atom states $|0\rangle|N_0\rangle$, $|i\rangle|N_0 - q_i\rangle$, $|E_\alpha^{\vec{k}}\rangle|N_0 - q_k\rangle$ for any integer q_k larger than $E_0/\hbar\omega$. The energy of the continuum states reached is nearly $q_k\hbar\omega + E_0$, with a spread depending on the intensity of the field and some atomic quantities. When peaks are observed in the electron energy spectrum, this spread is, of course, much smaller than $\hbar\omega$.

We expand the wave function of the atom-field system on the quasidegenerate dressed-atom states as

$$|\psi(t)\rangle = a_0(t)\,|0\rangle\,|N_0\rangle + \sum_i a_i(t)\,|i\rangle\,|N_0 - q_i\rangle + \sum_{q_k,\alpha} \int_{q_k\hbar\omega + E_0 - \epsilon}^{q_k\hbar\omega + E_0 + \epsilon} dE^k a_{E_\alpha^{\vec{k}}}(t) \times |E_\alpha^{\vec{k}}\rangle\,|N_0 - q_k\rangle \,, \tag{3}$$

where ϵ is much larger than the energy spread of each peak in the electron energy spectrum; ϵ^{-1} is chosen as much smaller than the shortest characteristic evolution time of $\psi(t)$.

By using the projection-operator techniques, we introduce an effective Hamiltonian acting only on the restricted basis $|0\rangle|N_0\rangle$, $|i\rangle|N_0 - q_i\rangle$, $|E_\alpha^{\vec{k}}\rangle|N_0 - q_k\rangle$ [see Eq. (3)]. The effective Hamiltonian matrix elements connect either two discrete states belonging to the set $\{|0\rangle|N_0\rangle, |i\rangle|N_0 - q_i\rangle\}$, a discrete state and a continuum state, or two continuum states. When continuum states are involved, matrix elements depend on the continuum states energy. Owing to the small magnitude of the energy spread of the peaks in the electron energy spectrum, we neglect the energy dependence of the Hamiltonian matrix elements involving continua. So we write $\hbar V_{ij}$, $\hbar K_{\alpha i}^{\vec{k}}$, and $\hbar L_{\alpha\alpha'}^{\vec{k}\,\vec{k}'}$, the matrix elements connecting, respectively, two discrete states i and j, a discrete state i and a continuum $(\vec{k},\alpha)$, and two continua $(\vec{k},\alpha)$ and $(\vec{k}',\alpha')$. The dipole matrix elements are chosen to be real.

The evolution of the wave function is governed by the equations

$$i\dot{a}_0 = \sum_i V_{0i}a_i + \sum_{q_k,\alpha} \int_{q_k\hbar\omega + E_0 - \epsilon}^{q_k\hbar\omega + E_0 + \epsilon} dE^k K_{\alpha 0}^{\vec{k}} a_{E_\alpha^{\vec{k}}} \,, \tag{4a}$$

$$i\dot{a}_i = \delta_i a_i + \sum_j V_{ij}a_j + \sum_{q_k,\alpha} \int_{q_k\hbar\omega + E_0 - \epsilon}^{q_k\hbar\omega + E_0 + \epsilon} dE^k K_{\alpha i}^{\vec{k}} a_{E_\alpha^{\vec{k}}} \,, \tag{4b}$$

$$i\dot{a}_{E_\alpha^{\vec{k}}} = \delta_{E^k} a_{E_\alpha^{\vec{k}}} + \sum_i K_{\alpha i}^{\vec{k}} a_i + \sum_{q'_{k'},\alpha'} \int_{q'_{k'}\hbar\omega + E_0 - \epsilon}^{q'_{k'}\hbar\omega + E_0 + \epsilon} dE^k L_{\alpha\alpha'}^{\vec{k}\,\vec{k}'} a_{E_{\alpha'}^{\vec{k}'}} \,, \tag{4c}$$

where

$$\hbar\delta_i = E_i - E_0 - q_i\hbar\omega$$

and (4d)

$$\hbar\delta_{E^k} = E^k - E_0 - q_k\hbar\omega \ .$$

By using the method initially introduced in Ref. 25 we derive the equations governing the evolution of the discrete part of the wave function:

$$|\tilde{\psi}\rangle = a_0(t)\,|0\rangle\,|N_0\rangle + \sum_i a_i(t)\,|i\rangle\,|N_0 - q_i\rangle \ . \tag{5}$$

Then we calculate the probabilities $P_\alpha^{\vec{k}}$ to reach the continuum $(\vec{k},\alpha)$.

Let us define the matrix $\mathscr{L}$ by its matrix elements $L_{\alpha\alpha'}^{\vec{k}\,\vec{k}'}$ and

$$\mathscr{N}_{\alpha i}^{\vec{k}} = \sum_{\alpha',\vec{k}'} [(1+i\pi\mathscr{L})^{-1}]_{\alpha\alpha'}^{\vec{k}\,\vec{k}'} K_{\alpha' i}^{\vec{k}'} \ . \tag{6}$$

$|\tilde{\psi}\rangle$'s components satisfy the equations

$$i\dot{a}_0 = \sum_i \mathscr{H}_{0i} a_i \ , \tag{7a}$$

$$i\dot{a}_i = \delta_i a_i + \sum_j \mathscr{H}_{ij} a_j \ , \tag{7b}$$

where

$$\mathscr{H}_{ij} = \mathscr{H}_{ji} = V_{ij} - i\pi \sum_{q_k,\alpha,\vec{k}} K_{\alpha i}^{\vec{k}} \mathscr{N}_{\alpha j}^{\vec{k}} \ . \tag{8}$$

$\mathscr{H}_{ij}$ defines a pseudo-Hamiltonian governing the evolution of $|\tilde{\psi}\rangle$. It is not Hermitian, its eigenvalues are complex. As a function of the light field flux $N_0\hbar\omega c$, each eigenvalue $\tilde{E}_i - i\tilde{\Gamma}_i$ can be followed by continuity so that the limit of $\tilde{E}_i - i\tilde{\Gamma}_i - (N_0 - q_i)\hbar\omega$, when N_0 is decreased to zero, is the energy E_i of the atomic state $|i\rangle$. $\tilde{E}_i - (N_0 - q_i)\hbar\omega$ is the light shift of the state $|i\rangle$, $2\tilde{\Gamma}_i/\hbar$ is its ionization probability at intensity $N_0\hbar\omega c$. The eigenvalue deduced from $|0\rangle$ corresponding to energy $\tilde{E}_0 - i\tilde{\Gamma}_0$ and the discrete part of the wave function are defined by the set of equations

$$(\tilde{E}_0 - i\tilde{\Gamma}_0)a_0 = \sum_i \mathscr{H}_{0i} a_i \ , \tag{9a}$$

$$(\tilde{E}_0 - i\tilde{\Gamma}_0)a_i = \delta_i a_i + \sum_j \mathscr{H}_{ij} a_j \ . \tag{9b}$$

The probability of reaching continuum $(\vec{k},\alpha)$ is given by

$$P_\alpha^{\vec{k}} = 2\pi \left| \mathscr{N}_{\alpha 0}^{\vec{k}} a_0 + \sum_i \mathscr{N}_{\alpha i}^{\vec{k}} a_i \right|^2 \tag{10}$$

when $|\tilde{\psi}\rangle$ is normalized at $t=0$, under the assumption of an adiabatic turning on of the field, i.e.,

$$|a_0(0)|^2 + \sum_i |a_i(0)|^2 = 1 \ . \tag{11}$$

For linearly polarized light, the $\vec{k}$ dependence of $P_\alpha^{\vec{k}}$ reduces to a dependence on θ, the angle between $\vec{k}$ and the light field polarization. Therefore, we study

$$P_{q_k}(\theta) = 2\pi \sum_\alpha P_\alpha^{\vec{k}} \tag{12a}$$

and

$$P_{q_k}^{\text{tot}} = \int_0^\pi P_{q_k}(\theta)\sin\theta\, d\theta \tag{12b}$$

which is the total ionization probability after absorption of q_k photons.

B. Application to cesium

According to the results obtained in Ref. 24, the initial state being $|6s\rangle\,|N_0\rangle$, we introduce the quasiresonant states $|7s\rangle\,|N_0-2\rangle$, $|6f\rangle\,|N_0-3\rangle$, and $|np\rangle\,|N_0-3\rangle$ with $9 \le n \le 12$. Atomic quantities are computed within the framework of a single-electron model (nonrelativistic) using a central potential. We have utilized an analytic potential depending on three parameters. The optimal potential is determined by minimizing the root-mean-square deviation between the zero-order calculated energies and the experimental ones.[26,27] Radial wave functions are obtained by numerical integration. The radial atomic part of the effective transition matrix elements is evaluated by means of the Dalgarno method[15,28] (see Appendix).

The ionization probabilities of the cesium ground state by absorption of four or five photons have been studied up to an intensity of 10^{12} W cm^{-2}. More precisely, we have calculated the probabilities $P_4(\theta)$, $P_5(\theta)$, P_4^{tot}, and P_5^{tot} [see Eq. (12)]. When intensity is weaker than 10^9 W cm^{-2}, four- and five-photon ionization probabilities vary, respectively, as I^4 and I^5 as predicted by perturbation theory applied at minimum nonvanishing order. In this range, the generalized cross sections

$$\sigma^{(p)}(\theta) = P_p(\theta)/I^p \tag{13a}$$

and

$$\sigma_{\text{tot}}^{(p)} = P_p^{\text{tot}}/I^p \tag{13b}$$

are constant. For higher intensities, the generalized cross sections become intensity dependent as described in Ref. 23. As an example, the variation of $\sigma^{(p)}(\theta=0)$ and $\sigma_{\text{tot}}^{(p)}$ are plotted in Fig. 1(a). The general trend is due to interferences between the quantum paths involving the quasiresonant states $9p$ and $10p$ and results in a strong decrease of the generalized cross sections at high intensity. A weak increase is observed until an intensity of 5×10^{10} W cm^{-2}, which corresponds to a two photon resonance of the $6s$-$7s$ transition.

It must be noted that the closest resonance in a weak field is the three-photon transition $6s$-$6f$. However, when the field intensity is increased, the frequency for the $6s$-$6f$ resonance is shifted away from ω, so that the contribution of quantum paths involving $6f$ becomes much smaller than the contributions involving p states.

Resonance effects do not modify four- and five-photon ionization cross sections exactly in the same way, and the ratios

$$R(\theta) = \sigma^{(5)}(\theta)/\sigma^{(4)}(\theta) \tag{14a}$$

and

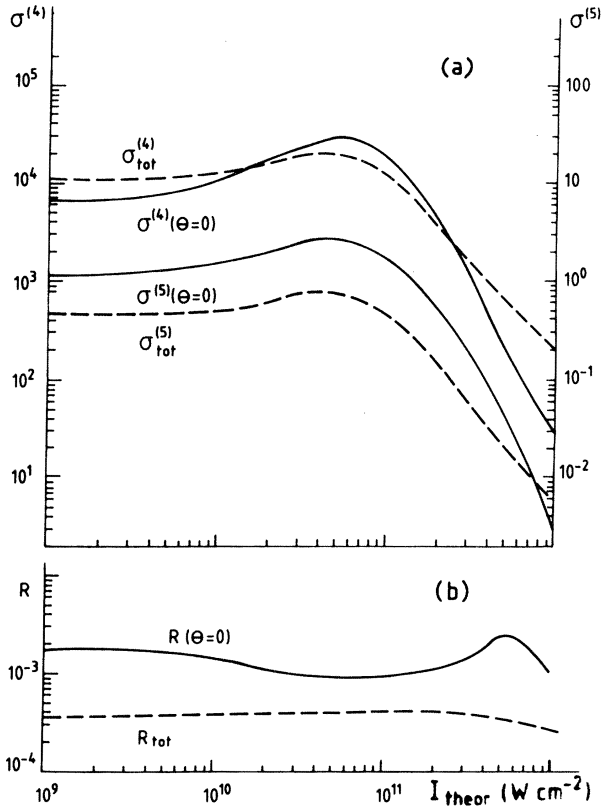

FIG. 1. (a) Differential $\sigma^{(p)}(\theta=0)$ and total cross sections $\sigma^{(p)}_{tot}$ for four- and five-photon ionization [in $s^{-1}/(GW\,cm^{-2})^p$] as functions of intensity [Eqs. (13)]. (b) Ratio of differential ($\theta=0$) and total five-photon to four-photon cross sections [Eq. (14)].

$$R_{tot}=\sigma^{(5)}_{tot}/\sigma^{(4)}_{tot} \tag{14b}$$

depend slightly on the field intensity. Their variations are plotted in Fig. 1(b) for $\theta=0$. Note that the modification is stronger on $R(\theta=0)$ than on R_{tot}.

Another evidence of resonance effects is provided by the study of angular distributions. In Figs. 2 and 3 the ratio $P_p(\theta)/P_p(0)$ is plotted for $p=4$ and 5, respectively. The structure of angular distribution is understood from Eq. (A12). The A_l's, B_l's, and C_l's are the probability amplitudes of reaching continuum l. As they correspond to different quantum paths, their intensity dependences are different and the angular distributions vary with intensity. Five-photon angular distribution keeps almost the same shape when the field intensity is varied from 10^9 to 10^{12} W cm^{-2}; this is related to the values of phase shifts which lead to strong cancellations except when θ is close to zero. On the contrary, four-photon angular distribution varies strongly in the intensity range 10^9–10^{12} W cm^{-2}. A four-lobe shape is obtained, characteristic of the fact that most electrons reach the d continuum. In a weak field the $\theta=0$ lobe has a structure: a shallow minimum at $\theta=0$ and a maximum near $\theta=20°$. This structure vanishes when an intensity of 10^{11} W cm^{-2} is reached and rebuilds for high intensity. At the same time, the $\theta=90°$ lobe lessens and extends again. This evolution

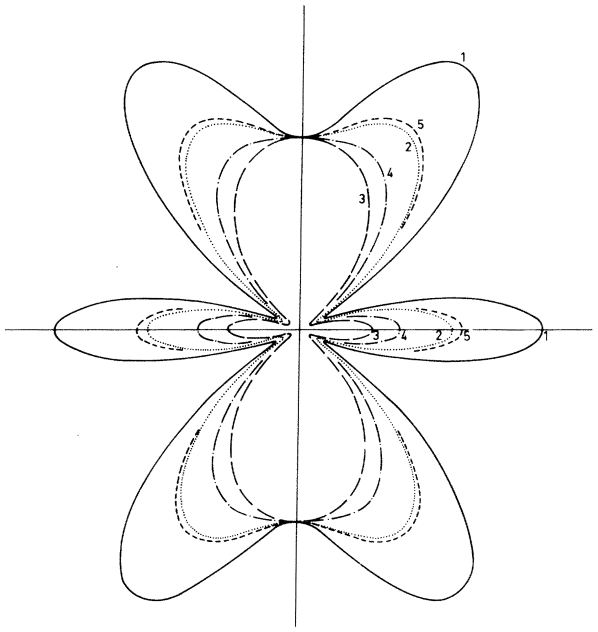

FIG. 2. Angular distributions for the four-photon ionization of cesium for different intensities (in W cm^{-2}): curve 1, 1×10^9; curve 2, 10^{10}; curve 3, 10^{11}; curve 4, 2×10^{11}; curve 5, 3×10^{11}.

is mainly related to the $6s$-$7s$ resonance which affects A_s and A_d but not A_g. This results in an increased probability of reaching the continua s or d rather than g.

C. Interpretation of experimental data

Experimentally, electrons are ejected after irradiation by a time-dependent field with a spatially dependent dis-

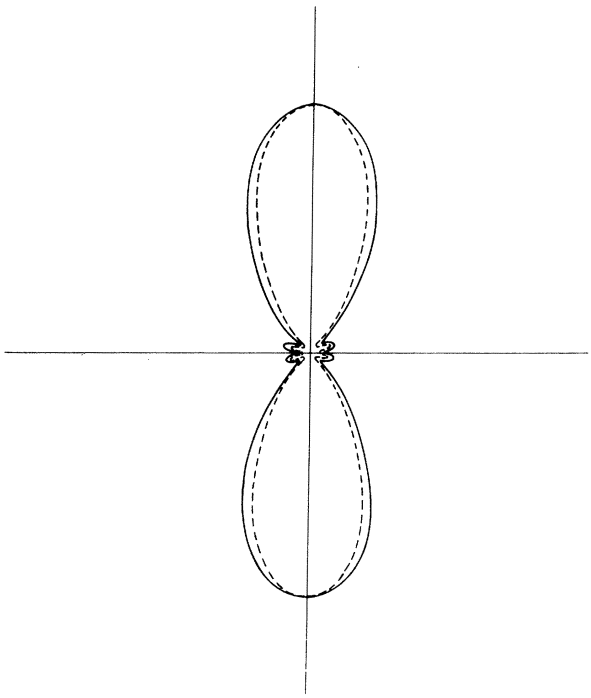

FIG. 3. Angular distributions for the five-photon ionization of cesium for two intensities: 10^9 W cm^{-2} (solid line), 10^{11} W cm^{-2} (dashed line).

tribution of intensity $I(r,t)$. We assume that an atom evolves adiabatically and thus follows the eigenstate deduced by continuity from the initial state. Our assumption is justified by the fact that eigenstates remain well isolated even near an anticrossing ($6s$-$7s$ resonance) in the intensity range up to 10^{12} W cm^{-2}. Ionization occurs with a time-dependent probability $P_4+P_5=2\Gamma_0$ so that the a_i's are proportional to

$$\exp\left[-\int_{-\infty}^{t}\Gamma_0[I(r,t')]dt'\right].$$

Contributions of each interaction volume element add to give the number of electrons detected. The number of electrons with energy nearly equal to $p\hbar\omega+E_0$ along the direction defined by θ is

$$N_p(\theta)=\int d\vec{r}\int_{-\infty}^{+\infty}dt\,P_p(\theta,I(r,t))\times\exp\left[-2\int_{-\infty}^{t}\Gamma_0(I(r,t'))dt'\right]. \quad (15)$$

The light field may be modeled by

$$I(\vec{r},t)=I_M\frac{e^{-r^2/a^2}}{\cosh(t/\tau)} \quad (16)$$

with $a=2.5\times10^{-3}$ cm and $\tau=(20.5\pm2.5)\times10^{-12}$ s.

From the ionization probabilities $P_4(\theta)$, $P_5(\theta)$, P_4^{tot}, and P_5^{tot}, we deduce the corresponding numbers of electrons $N_4(\theta)$, $N_5(\theta)$, N_4^{tot}, and N_5^{tot}. Only the latter quantities may be compared to experimental data and will be discussed in detail later. Qualitatively, in the low-intensity range, the effect of time and space integration is essentially to smooth the variations of the P's. Saturation occurs for intensities larger than 6×10^{10} W cm^{-2} so that the increase of the N's reflects only the extension of the interaction volume.[29] Once the saturation intensity is reached, the ratio N_5/N_4 and the angular distribution remain stable.

III. EXPERIMENTAL

The general experimental layout is presented in Fig. 4. A commercial picosecond Nd:YAG (yttrium aluminum garnet) laser system (Quantel, France) is focused in a cesium atomic beam in front of the input aperture of a time-of-flight electron spectrometer (Fig. 5).

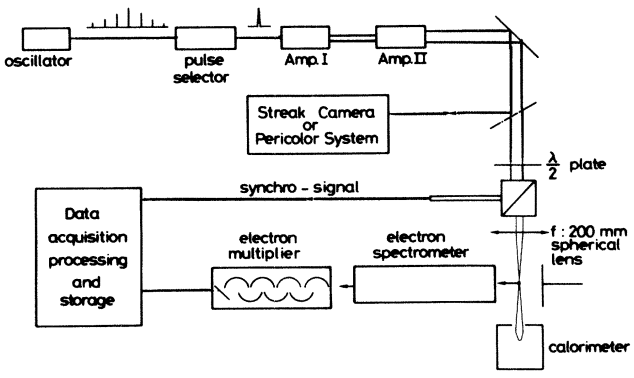

FIG. 4. General experimental layout.

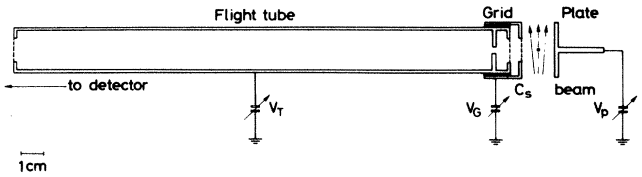

FIG. 5. Time-of-flight spectrometer.

A. The laser

The laser system consists in an oscillator delivering a train of about ten 50-ps [full width at half maximum (FWHM)] pulses. A single pulse of the train is selected and amplified by a two amplifiers system.

A real measurement of the maximum intensity, reached at the best focus, relies on three separate measurements of the pulse energy, the pulse duration, and the beam equivalent cross section at the best focus (see Ref. 2, Sec. III B 1 for a definition of this quantity. With the Gaussian beam shape assumed above, this section is simply equal to πa^2.) The pulse energy, averaged over a few tens of laser shots, is obtained from a measurement of the average laser power (Scientech 38-101) and from the pulse effective repetition rate. The repetition rate is ten pulses per second. About 10% of the shots are missed (probably due to the statistical behavior of the mode-locking dye) and another 10% is lost in the pulse selector. Therefore the effective repetition rate is closer, (8±1) Hz. The absolute calibration of the powermeter is subject to an uncertainty of 3% according to the specifications. The pulse duration was measured by means of a streak camera (Fig. 6), as described in Ref. 30, slightly modified to fit our 10-Hz repetition rate system. The pulse length measurements are averaged over a few tens of separate measurements. The standard deviation is taken as the error with a resulting (54±10) psec value. The intensity distribution in the focal plane of the lens was recorded after enlargement, on a silicium vidicon camera interfaced with an image fast digitizer (Pericolor, SEIN, France) as described in Ref. 31. The enlargement, obtained with a 20× microscope was directly measured by observing a micrometer and the area corresponding to 1 pixel was found to be 3.8×10^{-6} mm^2. The beam cross section, at the best focus, was measured to be 1.9×10^{-5}, 1.5×10^{-5}, and 1.35×10^{-5} cm^2 when using, respectively, two amplifiers, one amplifier, and no amplifier in the laser system. Note that using amplifiers or changing the pumping energy changes the rod's lens effect and moves the best focus po-

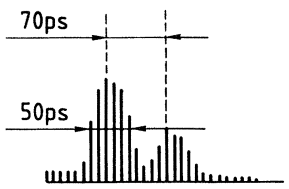

FIG. 6. Oscilloscope analysis of a vidicon image at the output of the streak camera. Lower pulse on the right is artificially produced and provides both time and intensity calibration.

sition (by 6 mm for the extreme situation). Therefore, to vary the intensity in a controlled manner this is not an allowable procedure. In this experiment the intensity was varied with a half-wave-plate—polarizer system as described in Ref. 10. The uncertainty of the beam cross section, as obtained from the standard deviation of measurements, was $\pm 10\%$.

Thus, in spite of the use of sophisticated techniques, the overall uncertainty of an absolute measurement of intensity is not better than $\pm(12.5+18+3+10)=\pm 43.5\%$ at a confidence level of 63%.

The problem of the pulse-to-pulse fluctuations was considered. This is important because we only measure the average energy, and thus an average value of the maximum intensity ($\langle I_M \rangle$). But a nonlinear process of order N will respond as I_M^N, so that everything will be as if the average intensity was $\langle I_M^N \rangle^{1/N}$ instead of $\langle I_M \rangle$. However, in our case, after averaging over 400 shots, which is much less than in the case of a real experiment, these quantities were not found to differ by more than 2%, so that this effect can be safely neglected (Fig. 7).

The main characteristics of our laser can be summarized as follows. Repetition rate is 10 Hz [(8 ± 1) Hz effective], maximum energy per pulse is 100 mJ, wavelength is 1.064 μm, and pulse length is (54 ± 10) ps. The beam section at focus ($f=200$ mm) is, with just the oscillator, 1.35×10^{-5} cm^2; with one amplifier, 1.5×10^{-5} cm^2; and with two amplifiers, 1.9×10^{-5} cm^2.

B. Atomic beam

Given our laser pulse length and the intensity range we use, the problem of dimers was not critical.[32] However, we chose to use a cesium beam apparatus where the oven and nozzle temperatures could be separately controlled. Typical operating temperatures were between 30 and 120 °C for the oven and 300—600 °C for the nozzle. Densities in the beam were estimated to be a few 10^9 cm^{-3}.

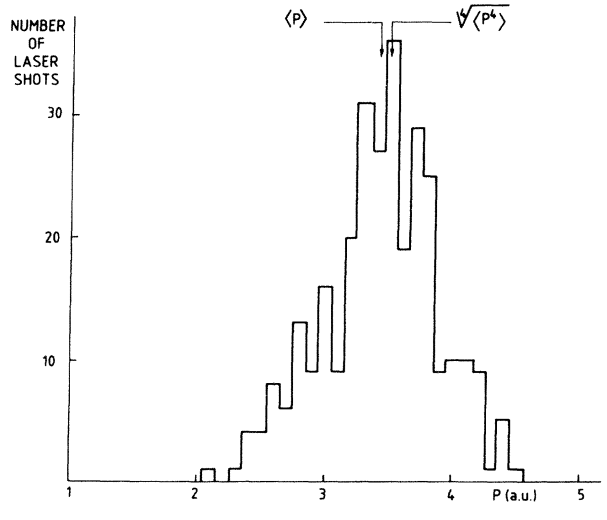

FIG. 7. Peak power amplitude distribution for about 400 laser shots. Average value $\langle P \rangle$ is the one used in the determination of the intensity. Effective power $(\langle P^4 \rangle)^{1/4}$ for a four-photon process is shown for comparison.

Throughout the experiment, no signal which could possibly originate from dimers was ever detected.

C. Electron energy analyzer

The nature of our electron signal is well fit to the use of a time-of-flight spectrometer whose resolution, on the other hand, is quite enough for our needs (15 meV reported in Ref. 33). Therefore, we used a modified version of the time-of-flight spectrometer which had been long used in MPI experiments to separate different ionic species. This instrument is represented on Fig. 5. The time-of-flight region itself consists of $8\frac{1}{2}$-in (21.6-cm) long Netic-Conetic tube, ended by two grids (0.9-mm mesh, transmission $>90\%$), electrically isolated from the ground so that its potential V_T can be chosen by the experimenter. The atomic density in the beam was about 5×10^9 cm^{-3} and an electron density of the same order is expected at saturation. The Debye length for an electron energy of 0.8 eV is then 70 μm, only a few times larger than our laser-beam focus size (25 μm) so that a complete charge separation is not obtained at all intensities.

To eliminate differences between the collection efficiency for the two species of electrons due to the influence of space charge which would be very difficult to estimate, we place the interaction region in a separation field produced by a negative voltage (V_P) applied to a plate set in front of the flight tube. In order to make the separation field independent of the potential of the flight tube, a second grid G (potential V_G) is added between the laser focus and the entrance grid of the flight tube. This arrangement allows us to choose independently the separation field and the energy of the electrons inside the flight tube which ultimately determines the energy resolution of the analyzer. Finally, we found it necessary to add a 2-mm-diam pinhole to eliminate noise electrons produced, most probably, by stray light hitting the plate P. This hole was placed inside the flight tube, in the field-free region, to avoid an electrostatic lens effect which would have occurred if this pinhole had been used in replacement of one of the grids, for instance.

Shielding against the Earth's magnetic field is achieved by enclosing the whole system in a Netic-Conetic box. However, some apertures are necessary to introduce the cesium beam, laser beam, and extract the electrons. Therefore the shielding is not perfect. Inside the tube, for instance, stray fields of a few tens of mG (at most, close to the output grid) have been measured. All the metallic parts are plated with gold to eliminate contact potentials.

The energy resolution of this spectrometer, albeit not high, is quite sufficient to analyze the structure expected for MPI of cesium: a sample of such a spectrum is shown in Fig. 5 where two lines separated by 1.17 eV (the photon energy) are clearly resolved. The angular resolution if somewhat more difficult to evaluate since it depends on the applied voltages. To reach the detector, the electron velocities must deviate by less than 1.3° from the tube axis. Computer analysis of electron trajectories shows that the collection angle depends on $\alpha=V_T/E_K$ (where V_T is the tube voltage and E_K the initial kinetic energy of the electrons produced at ground potential). For moderate

values of α (say, $\alpha<4$) the collection half-angle ϕ_0 remains smaller than 3°. The collection efficiency, proportional to ϕ_0^2, therefore depends on α and the measurements must be corrected for this variation. Moreover, the collection efficiency depends also on the electron kinetic energy inside the flight tube $E_A=E_K+V_T$, probably because of a stray magnetic field. Comparison of signals at different kinetic energies E_K is possible only if the analysis energy E_A is kept constant. When E_A is kept large enough (typically above 2 eV), the dependence of the collection efficiency towards V_T agrees rather well with the α dependence discussed above. This point will be considered again when discussing the relative value of five- and four-photon ionization cross sections in Sec. V.

No precise absolute energy calibration was performed because of unknown time delays in the detection electronics and contact potentials (although minimized). Relative energy calibration is easily achieved by changing V_T which results in equal shifts of the electron kinetic energies: If this change is equal to 1.17 eV the "slow" peak appears in the channels where the "fast" one was. This allows an identification of the lines in Fig. 8.

D. Data-acquisition system

After exiting the flight tube, the electrons are collected on the cathode of an electron multiplier (57 P 17-2, Radio Technique Compelec), amplified and fed to an electron-counting system. The counting scale is based on high-speed shift registers which transfer into 256 channels, corresponding to a time interval programmable from 10 ns to 2.56 μs each, the pulses generated by the detection of a single electron. A microprocessor handles the accumulation. The triggering signal is supplied by the laser pulse detected by a photodiode. The results of an accumulation (a typical run will accumulate a few thousand laser shots) can be passed on to a Digital Equipment Corp. LSI-11 type computer which handles the storage on a floppy disc and eventually, the data processing.

IV. ANGULAR DISTRIBUTIONS

In a preliminary experiment, we first observed the ion signal in order to remove all ambiguity concerning the electron signal. To this end, the plate P was set to a high positive voltage so that all the ions were collected on the electron multiplier cathode, the flight tube acting as a mass spectrometer.

An ion signal was observed and both the timing of this signal and the intensity dependence (experimental order of nonlinearity, see details in Sec. V) proved that it was due to cesium MPI. No signal due to dimers could be detected, nor any significant noise signal (other impurities, surface emission, etc.), so that it can be safely said that the quasitotality of the electron signal was due to cesium MPI.

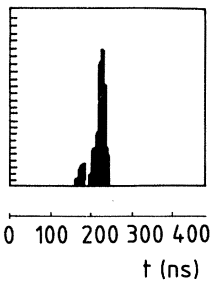

FIG. 8. Typical time-of-flight spectrum from MPI of cesium.

Then the electron signal was observed, and spectra like the one in Fig. 8 were taken. A typical voltage setting for such a spectrum would be $V_P=-10$ V, $V_G=10$ V, $V_T=2$ V. Of course, it is necessary to make sure that the electrons are created at the ground potential, which may require a minor shift of both V_P and V_G and/or some lens focus lateral adjustment.

A. Angular-distribution measurements

Angular distributions of photoelectrons are very simply measured, in the case of linearly polarized light, by rotating the laser polarization in a plane perpendicular to the light propagation.[16–21] This was done in our experiment by inserting a half-wave plate between the Glan prism and the focusing lens (see Fig. 1). For each position of the half-wave plate, a spectrum like the one in Fig. 5 was taken, and the average number of electrons per laser shot was computed separately for each peak. Every third run, a spectrum in the direction of the light polarization is taken, which is used to normalize our angular distributions, thus accounting for a possible drift of the signal.

Measurements were made for two different laser intensities, 6×10^{11} and 8×19^{9} W cm^{-2}. High-intensity measurements were made using the laser described in Sec. III, but for low intensities, the count rate was too low to allow the use of a picosecond pulse. Therefore, the laser was modified to deliver a single longitudinal 40 ns pulse (similarly to the one described in Ref. 10), its other characteristics being left unchanged.

B. Experimental data

The results of these measurements are shown in Figs. 9 and 10. High-intensity results are shown on Fig. 9. The abscissa is the angle θ between the laser polarization and the electron detection direction. The ordinate is the ratio of the count per laser shot in the direction given by θ to the same count per laser shot at $\theta=0$.

Figures 9(a) and 9(b) show the results obtained at high intensity (6×10^{11} W cm^{-2}) for four- and five-photon ionization, respectively. The error bars reflect the dispersion of the results obtained over several measurements. The lines are the results of a calculation of angular distribution, as discussed in Sec. I, under the experimental conditions.

Figure 10 is similar to Fig. 9(a) but has been obtained at a laser intensity of 8×10^{9} W cm^{-2} with the nanosecond pulse. The two lines correspond to distributions calculated for 8×10^{9} and 16×10^{19} W cm^{-2}.

In the high-intensity region, the angular distributions are rather insensitive to the intensity and mainly reflect that obtained at the saturation intensity. This is no longer true in the case of Fig. 10. The choice of 8 and 16 GW cm^{-2} corresponds to the intensity measured experi-

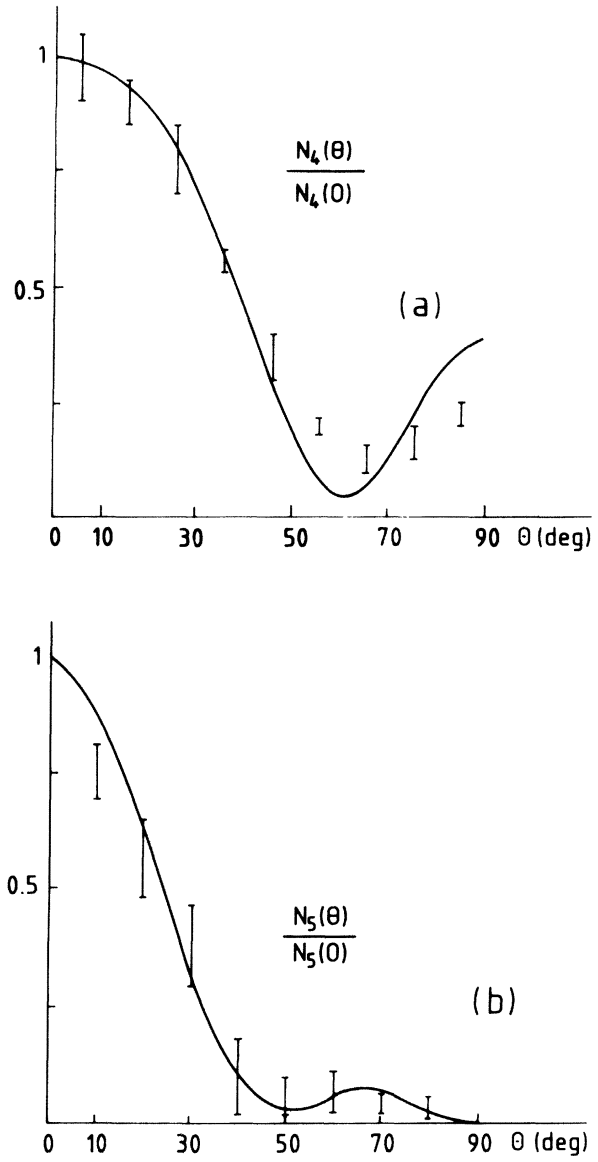

FIG. 9. (a) Angular distribution $N_4(\theta)/N_4(0)$ recorded at $I=6\times10^{11}$ W cm^{-2}. Solid line has been calculated using the parameters of Table I. (b) Angular distribution $N_5(\theta)/N_5(0)$ recorded at $I=6\times10^{11}$ W cm^{-2}. Solid line has been calculated using the parameters of Table II.

mentally and to the one giving the best overall fit between theory and experiment (see Sec. V). For intensities in the GW cm^{-2} range, no extra ATI peak was observed.

C. Discussion

Theoretical angular distributions are calculated from the N's given by Eq. (15). For intensities weaker than 10^{11} W cm^{-2}, the shapes obtained for $N_p(\theta)/N_p(0)$ are almost identical to the ones obtained for $P_p(\theta)/P_p(0)$. Because of saturation, the integrated angular distributions do not change when the field intensity becomes larger than 10^{11} W cm^{-2}.

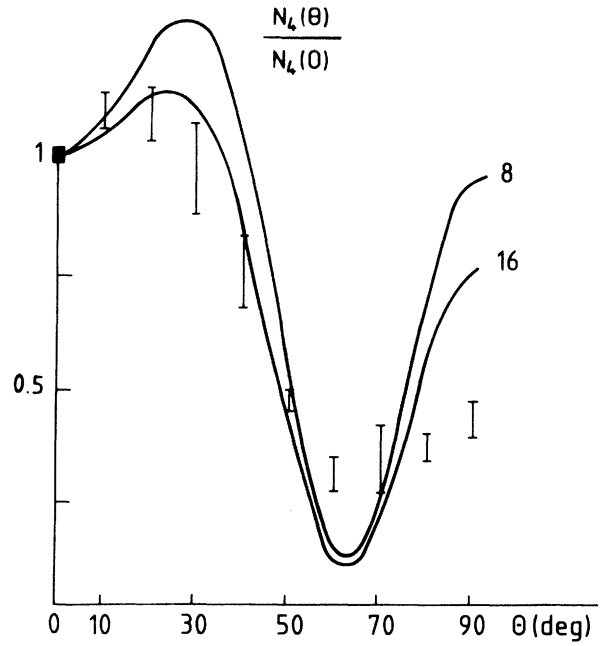

FIG. 10. Angular distribution $N_4(\theta)/N_4(0)$ recorded at $I=8\times10^9$ W cm^{-2}. Solid lines are calculated using the coefficients of Table I and intensities of 8 and 16 GW cm^{-2}.

By absorption of four photons, continua s, d, and g are reached. Angular distributions in these continua are characterized by the number of lobes: isotropic for s, four lobes for d, and eight lobes for g. Experimentally and theoretically we obtain four-lobe distributions. The structure of the principal lobe (shallow minimum at $\theta=0$ between two maxima at $\theta=\pm20°$) mentioned in Sec. II is observed experimentally. Likewise, the secondary lobes ($\theta=90°$) are found to be smaller in a strong field than in a weak field. So the salient features of experimental four-photon angular distributions are reproduced by our calculation.

Angular distributions are described by Eq. (A12a) and depend on six quantities: three A's and three phases. Theoretical phases, investigated by various techniques, may be considered as very reliable. For a more precise comparison between calculation and experimental data we have used Eq. (A12a) to obtain "experimental" values of the A's. Theoretical phases are used and the A's are treated as parameters to obtain a best fit between Eq. (A12a) and experimental points. The results are given in Table I.

The A's are normalized so that $N_4(\theta=0)=1$. The main difference concerns the contribution of ionization to continuums, the experimental value of A_s/A_d being larger than the theoretical one by a factor of about 2, while the experimental and theoretical values of A_g/A_d remain similar.

By absorption of five photons, continua p, f, and h are reached corresponding, respectively, to angular distributions with 2, 6, and 10 lobes. Experimental as well as theoretical distributions have essentially two lobes, with a pronounced maximum for $\theta=0$. This maximum is too thin to be a p lobe. It appears that the contributions of

TABLE I. Four-photon ionization. Relative values of A_l [Eq. (A12a)] normalized so that $N_4(\theta=0)=1$. For a weak field [Fig. 9(a)] and a strong field (Fig. 10), theoretical predictions of A_l are compared with the result of a fit between Eq. (A12a) and experimental points.

	Weak field			Strong field	
		Theory			Theory
	Expt.	(8×10^9 W cm^{-2})	(18×10^9 W cm^{-2})	Expt.	(4×10^{11} W cm^{-2})
A_s	−0.54	−0.35	−0.32	−0.39	−0.25
A_d	0.45	0.69	0.62	0.41	0.51
A_g	−0.12	−0.25	−0.19	−0.05	−0.09

ionization to continua p and f are dominant and strongly cancel each other so that the side lobes almost vanish.

The angular distribution is described by Eq. (A12b). The number of atomic quantities (B's, C's, etc.) appearing is too large for their determinations to be significant. So we have calculated five-photon angular distributions as quadratic forms, in Y_1, Y_3, and Y_5, and we compare the experimental and theoretical values of the coefficients of Y_1^2, Y_3^2, Y_5^2, Y_1Y_3, Y_1Y_5, and Y_3Y_5.

As in Sec. IV C, experimental coefficients are obtained by fitting experimental data and the result of Eq. (A12b). The coefficients are normalized so that $N_5(\theta=0)=1$. The comparison is illustrated by Table II.

Note that from the parametric study of experimental data we deduce the ratios $N_p(\theta=0)/N_p^{\text{tot}}$. Anticipating Sec. V, this result allows us to calculate an experimental value of the ratio $N_5^{\text{tot}}/N_4^{\text{tot}}$.

V. ABOVE-THRESHOLD IONIZATION

In this section, we put the emphasis on the intensity dependence of the different peaks of our electron spectrum. All the electron measurements are made for $\theta=0$, that is, for the electrons propagating along the laser polarization.

Three different types of measurements will be reported in this section. We first measured the experimental order of nonlinearity for the different processes which can be observed in our experiment. We then observed the intensity behavior of our electron spectrum in the saturation region, and, finally, made a careful measurement of the amplitude ratio of the two peaks in the saturation region.

TABLE II. Five-photon ionzation. According to Eq. (A12b), $N_5(\theta)/N_5(0)$ is a quadratic homogeneous function of Y_1, Y_3, and Y_5. Theoretical predictions for the coefficients are compared to the result of a fit with experimental points.

	Coefficient	
Term	Expt.	Theory
Y_1^2	0.051	0.046
Y_3^2	0.079	0.091
Y_5^2	0.0012	0.0014
Y_1Y_3	0.088	0.098
Y_1Y_5	−0.010	−0.016
Y_3Y_5	−0.0070	−0.017

A. Experimental order of nonlinearity

This quantity is defined as[2]

$$K_{\text{expt}}=\frac{\partial \ln n}{\partial \ln I}$$

(N is the number of particles—electrons or ions—detected and I is the laser intensity). It is important because, in a process which can be described by LOPT, it is equal to the number of photons absorbed in the process. It has to be measured for intensities well below the saturation intensity.

K_{expt} was separately measured for the ion signal and for the two electron peaks. If no particular problems were met in the case of the ions, this was not the case for the electrons. Because our apparatus was angle selective for the electrons (and not for the ions which are all collected), the signal was too low in the low-intensity region to make a good measurement of K_{expt} possible. Therefore, the signal was increased by defocusing the laser, which leads to an increase of the interaction volume. A severe drawback of this method has to be mentioned: the laser intensity cannot be precisely measured, only its order of magnitude (of course, its variations are well known). The measured values of the experimental order of nonlinearity are given in Table III together with the results obtained for the ion signal.

The fact that the measured K_{expt} were close to 4, 4, and 5 (the number of photons absorbed in each process) gave us total confidence in the identification of our signals even though the situation is more complicated than that described by LOPT.

Since this issue is addressed by K_{expt} measurements, it

TABLE III. Experimental and calculated values of $K_{\text{expt}}=\partial \ln N/\partial \ln I$; laser intensities are in the range 3×10^{11}–6×10^{11} W cm^{-2}.

Source	Ions (total)	Slow electrons ($\theta=0$)	Fast electrons ($\theta=0$)
Expt.	3.85±0.2	4.2±0.2	4.8±0.2
Theory	4	4.3	5

is important to give at least an order of magnitude of the intensity used in this part of the experiment. It was estimated to be between 3×10^{10} and 6×10^{10} W cm^{-2}.

As we mentioned in Sec. II, the variation of the ionization probabilities is not governed by a power law in the range where K_{expt} has been measured. Thus the experimental values of K_{expt} have to be compared to the slope of tangent to the curves log$N$ versus log$I$ for measured intensities. As shown by Fig. 1, in the range 3×10^{10}–6×10^{10} W cm^{-2} the four- and five-photon cross sections increase slightly for $\sigma^{(4)}_{tot}$, $\sigma^{(5)}_{tot}$, and $\sigma^{(5)}(\theta=0)$, more strongly for $\sigma^{(4)}(\theta=0)$. The measured number of ions is proportional to $N_4^{tot}+N_5^{tot}$ [Eq. (15)] while the number of slow (fast) electrons is proportion to $N_4(\theta=0)$ $[N_5(\theta=0)]$. As already mentioned, the effect of time and space integration for moderate intensities is to smooth the intensity dependence of ionization probabilities. For intensities of 3×10^{10}–6×10^{10} W cm^{-2}, N_4^{tot}, N_5^{tot}, and $N_5(\theta=0)$ vary as I^4, I^5, and I^5, respectively, while $N_4(\theta=0)$ varies as $I^{4.3}$. These results are in good agreement with observed effective orders of nonlinearity.

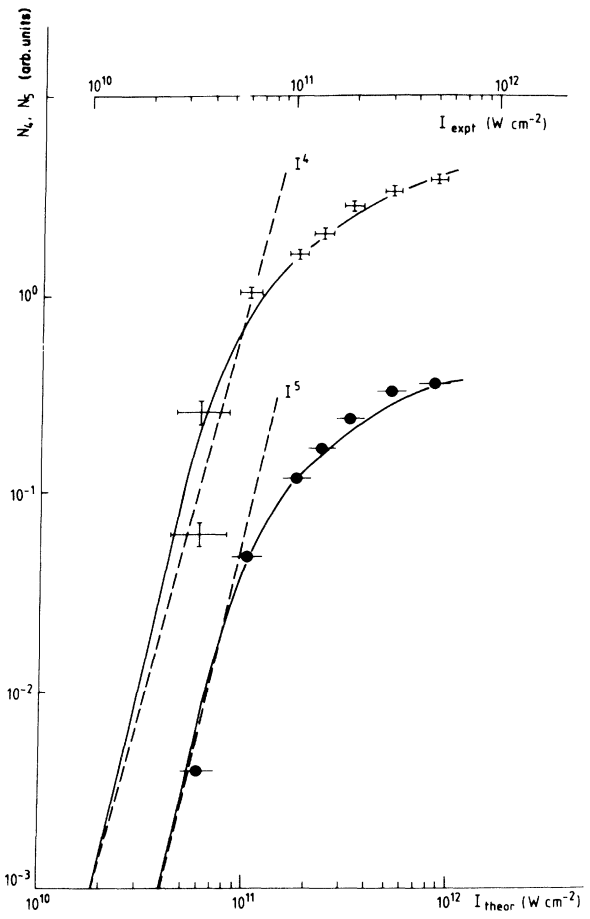

FIG. 11. $N_4(\theta=0)$ and $N_5(\theta=0)$ in arbitrary units as functions of intensity. Crosses and circles are experimental. Solid lines are calculated. Dashed straight lines of slope 4 and 5 are shown for comparison. Note the different experimental (I_{expt}) and theoretical (I_{theor}) intensity scales.

B. The saturation region

With the laser focused in front of the spectrometer aperture, only the saturation region of the electron signal can be studied. This is simply done by computing the count per laser shot on each peak from spectra like the one of Fig. 5, taken at different laser intensities. In Fig. 11, these counts are plotted against the laser intensity. The top curve corresponds to the slow electrons, the bottom one to the fast ones. The points are experimental and the full lines are the results of the calculations of Sec. I, superimposed by a double translation (horizontal and vertical). The vertical translation is justified by the fact that the experimental points are obtained in arbitrary units only. However, this translation was not enough to bring the experimental points onto the theoretical curves. In other words, the experimental results look identical to the theoretical one, but for a different intensity. This is indicated on Fig. 11 by the use of two intensity scales: on top, the axis is marked off in intensity as resulting from our measurements, the bottom one in "theoretical intensities." It looks like the "experimental intensity" was underestimated by about 80%, which is about twice our error bar on the intensity, although there is no systematical error in the measurements we can think of.

It must be made clear that though the two series of experimental points were independently fitted to theoretical curves, the same intensity scale is used for both curves. Thus Fig. 11 emphasizes the excellent agreement between experimental and theoretical intensity behaviors of the ionization probabilities in the saturation region.

C. Probability ratio of the five- and four-photon MPI processes

Variations of the electron spectrometer transmission with the electron energy have to be taken into account if one seeks to measure a probability ratio for the five- and four-photon ionization of cesium. These variations are caused first by the variation of the collection angle with the electrons initial kinetic energy (when the electrons are accelerated between the focus and the tube), and also by the variations of the transmission of the flight tube itself with the electron kinetic energy inside the tube. As seen in Sec. III, the collection angle is simply computed from the values of V_T and the electron initial kinetic energy. Variations of the flight-tube transmission are more complicated to deal with but they are important only for low kinetic energies inside the tube because they are most probably due to stray magnetic fields, which are rather weak. Moreover, a simple way of getting around this problem is to measure the two peak amplitudes at the same energy inside the flight tube. Thus the experimental procedure for measuring the absolute probability ratio is as follows. A first spectrum is taken at a given value of V_T and the count per laser shot is measured on the fast electron peak. Then V_T is increased by one photon energy and the experiment is repeated to measure the count per laser shot on the slow electron peak. These counts now just have to be corrected by the relevant collection factor. Note that these corrections are intensity independent so that they need to be measured for one point of the curves

of Fig. 11 only.

We chose the highest possible intensity (rightmost point on the figure) because, due to saturation, the ratio in this region is almost intensity independent. Eight sets of two spectra (for values of V_T differing by 1.17 eV, as explained above) were taken for different values of V_P, V_G, and V_T. The absolute ratio of the fast to slow electron signal was determined giving an average value of 6.8×10^{-2}, with a standard deviation of 1×10^{-2}. This compares to a theoretical value of 8.8×10^{-2}. We would like to point out that the dispersion of the measurement is less than 15% of the average. Given the total count on both peaks of the spectra this simply reflects the statistical dispersion. In particular, no special behavior of the ratio towards the potentials (V_P, V_G, and V_T) could be determined, the points being statistically scattered.

These corrections were incorporated in Fig. 12 which shows the dependence of the ratio of the five-photon to four-photon electron counts towards the laser intensity. The same double intensity scale as in Fig. 11 is used, but the ratio (experimental) is now given in absolute units. The top solid line is the ratio calculated for electrons emitted along the laser polarization, the bottom one is the result of the same calculation for the total ionization.

If we ignore the discrepancy between experimental and theoretical intensity scales, our calculation reproduces rather well the saturation of ionization probabilities. The shape of the curves plotted in Figs. 11 and 12 depends essentially on the total ionization probability. The parametric study of angular distributions (Sec. IV) allows us to calculate the ratios $N_5^{\rm tot}/[4\pi N_5(\theta=0)]=0.14$ and $N_4^{\rm tot}/[4\pi N_4(\theta=0)]=0.33$. The ratio $N_5(\theta=0)/N_4(\theta=0)$ has been directly measured to be 6.8×10^{-2}. From these three ratios we deduce an experimental value of $N_5^{\rm tot}/N_4^{\rm tot}=(2.9\pm0.5)\times10^{-2}$. We have not introduced an error bar corresponding to the ratio $N_p^{\rm tot}/N_p(\theta=0)$ since it is expected to be much smaller than the error bar on $N_5(\theta=0)/N_4(\theta=0)$. The corresponding point is placed on the bottom curve of Fig. 12. The theoretical prediction of 3.3×10^{-2} is now in the experimental error bar. Finally, the data which depend mostly on total ionization probabilities (the latter ratio and the saturation shapes illustrated by Fig. 11) are in better agreement than the angle-dependent data. This is not a surprise and confirms once more the great sensitivity of angular-distribution measurements.

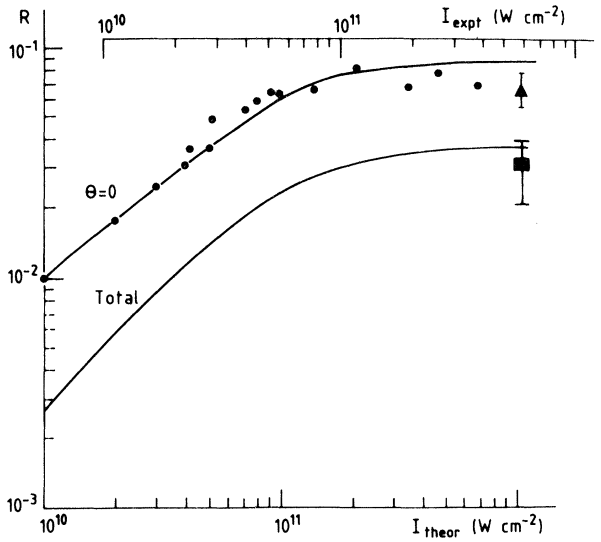

FIG. 12. Ratio N_5/N_4 as a function of intensity. Experimental values (dots) are normalized to the value at 6×10^{11} W cm^{-2} discussed in the text. Solid lines are theoretical. Note again the different intensity scales. Experimental point on the lower curve gives the experimental determination of the total signal ratio resulting from our angular-distribution measurements.

VI. CONCLUSION

The new effects discussed in this paper which appear in cesium MPI under high laser intensities are of two kinds: those concerning ATI and those concerning the angular distributions.

Though ATI has been studied for some time now, this is the first time that a measurement of the relative ATI probabilities was made in a situation where a comparison with the theory is possible. This is also the first complete calculation accounting for realistic experimental conditions and the result of the comparison is quite satisfactory.

Concerning the question whether LOPT can be used or not, we note that if higher-order corrections had to be included to satisfactorily account for some of the experimental features (four-photon experimental order of nonlinearity at $\theta=0$, saturation shape, absolute value of the ionization probability ratio), the nature of these corrections (Stark shift of bound states) has been known for long. As already seen in Ref. 24, when high intensities are used, these terms have to be included in the calculations even if the ionization process is, in the low-field limit, nonresonant. On the other hand, some effects of very high intensities such as strong differences between $K_{\rm expt}$ and the number of photons absorbed[11] or important variations of the ionization threshold[34] have not been observed here, because they occur at still higher intensities. Note that a good knowledge of ATI processes is a necessary step in the understanding of new kinds of MPI processes currently under study such as double ionization.[35]

Concerning the angular distributions, we can say that, again, the intensity dependence is well predicted even if in the case of the four-photon ionization some discrepancies are observed in the shape of the angular-distribution curves. The agreement is very good in the case of five-photon ionization. Once again the intensity behavior is governed by the Stark shifts of nonresonant bound states.

One of the key results of the paper is that all the features depending on the total ionization cross section are much more easily reproduced than those depending on angular parameters. Angular distribution is thus shown to be a very sensitive tool in such studies.

Improvements in this comparison between theoretical and experimental results can be expected in two directions. On the experimental side, better measurements of the space-time intensity repartition are certainly needed. However, they represent a tedious task and would most

probably bring only a small improvement to the comparison. The theory would certainly be improved by taking into account relativistic effects, which could be of capital importance concerning the four-photon ionization angular distribution. However, it can be said now that the question of the multiphoton ionization of atoms with a single valence electron is well understood whatever the intensity or the pulse duration is, within the present experimental possibilities.

ACKNOWLEDGMENTS

The authors would like to acknowledge the help of D. Fondant for his technical assistance and thank J. Thebault for his help during the laser-intensity measurements.

APPENDIX

The probability of reaching continuum $(\vec{k},\alpha)$ is given by Eq. (10):

$$P_\alpha^{\vec{k}} = 2\pi \left| \sum_j \mathcal{M}_{\alpha j}^{\vec{k}} a_j \right|^2 , \tag{A1}$$

where j stands for initial or resonant discrete states.

The matrix elements involved in the determination of the $\mathcal{M}_{\alpha j}^{\vec{k}}$ [Eq. (6)] and in the effective Hamiltonian $\mathcal{H}_{ij}$ [Eq. (8)] leading to the determination of the a_i components of the wave function are calculated by perturbation theory at minimum nonvanishing order. As far as total ionization probabilities are concerned, the procedure used to calculate atomic quantities involved in these matrix elements has been described in detail in Refs. 14, 15, and 27. For differential ionization probabilities, calculation of matrix elements between discrete states remains unchanged and here we only consider matrix elements involving, as a final state, the continuum $|E_\alpha^{\vec{k}}\rangle$ state. This state, which must represent asymptotically a plane wave with momentum k plus incoming waves,[36] may be written as

$$|E_\alpha^{\vec{k}}\rangle = \sum_{l_\alpha} i^{l_\alpha}(2l_\alpha+1)e^{-i\varphi_{l_\alpha}} R_{kl_\alpha}(\vec{r}) P_{l_\alpha}(\vec{k}\,\vec{r}) , \tag{A2}$$

where P_l are Legendre polynomials. The atomic radial wave functions $R_{kl_\alpha}(r)$ normalized per unit Rydberg energy have the asymptotic form

$$R_{kl}(r) = k^{-1/2} \sin\left[kr - \frac{\pi l}{2} + \frac{1}{k}\ln(2kr) + \varphi_{l_\alpha} \right] , \tag{A3}$$

where φ_{l_α} is the phase shift of the l_αth partial wave.

Discrete states are expanded in spherical harmonics

$$|i\rangle = R_{nl}(r) Y_{lm}(\vec{r}) . \tag{A4}$$

Matrix elements between an initial state j (ground state or resonant discrete state) and $|E_\alpha^k\rangle$ are of the form

$$J_{j\alpha}^{\vec{k}} = \sum_{\{\alpha_i\}} \frac{\langle j|D|\alpha_1\rangle\langle\alpha_1|D|\alpha_2\rangle\cdots\langle\alpha_p|D|E_\alpha^k\rangle}{\hbar\Delta_1\hbar\Delta_2\cdots\hbar\Delta_p} , \tag{A5}$$

where D is the dipole operator

$$D = rC_0^{(1)}(\vec{r}) . \tag{A6}$$

The sums run over atomic bound and continuum states. The Δ_j denominators defined by Eq. (4d) are given by

$$\Delta_j = E_j - E_0 - q_j\hbar\omega . \tag{A7}$$

When above-threshold ionization is concerned, the last Δ_p quantity vanishes in the integration over continuum states and $J_{j\alpha}^{\vec{k}}$ quantities are calculated by using the formula

$$\lim(D - i\eta)^{-1} = PD^{-1} + i\pi\delta(D) \tag{A8}$$

as explained in Ref. 4. P represents a Cauchy principal value integration.

Due to properties of spherical harmonics,[37] the $\vec{k}$ dependence of $J_{j\alpha}^{\vec{k}}$ can be separated from the angular and radial part $R_{j\alpha}(\vec{r})$ and one obtains

$$J_{j\alpha}^{\vec{k}} = R_{j\alpha}(\vec{r}) e^{-i\varphi_{l_\alpha}} Y_0^\alpha(\vec{k}) \tag{A9}$$

when the initial state is an s state. $R_{j\alpha}(\vec{r})$ accounts for the various quantum paths between the initial and final state. The infinite summation involved in radial matrix elements are avoided by the use of perturbed-functions solutions of the inhomogeneous single-particle differential equation as detailed in Refs. 15 and 27. $R_j\alpha(\vec{r})$ is real when the lowest continuum is concerned, and complex when above-threshold ionization is studied.

The expression for differential and total ionization probabilities towards the continua reached after the absorption of four or five photons may be written as

$$P_4^{\vec{k}} = \left| \sum_{l=0,2,4} A_l e^{-i\varphi_l} Y_0^l(\vec{k}) \right|^2 , \tag{A10a}$$

$$P_5^{\vec{k}} = \left| \sum_{l=1,3,5} (B_l + iC_l) e^{-i\varphi_l} Y_0^l(\vec{k}) \right|^2 , \tag{A10b}$$

where A_l, B_l, and C_l are real quantities. Using the well-known relation

$$Y_0^L(\vec{k}) = \left[\frac{2L+1}{4} \right]^{1/2} P_L(\cos\theta) , \tag{A11}$$

one obtains the expressions of $P_p(\theta)$:

$$P_4(\theta) = \frac{1}{2} \left| \sum_{l=0,2,4} A_l e^{-i\varphi_l} \sqrt{2l+1} P_l(\cos\theta) \right|^2 , \tag{A12a}$$

$$P_5(\theta) = \frac{1}{2} \left| \sum_{l=1,3,5} (B_l + iC_l) e^{-i\varphi_l} \sqrt{2l+1} \times P_l(\cos\theta) \right|^2 , \tag{A12b}$$

and

$$P_4^{\text{tot}} = \sum_{l=0,2,4} A_l^2 , \tag{A13a}$$

$$P_5^{\text{tot}} = \sum_{l=1,3,5} |B_l + iC_l|^2 , \tag{A13b}$$

[1]F. V. Bunkin and A. M. Prokhorov, Zh. Eksp. Teor. Fiz. 46, 1090 (1964) [Sov. Phys.—JETP 19, 739 (1964)].
[2]J. Morellec, D. Normand, and G. Petite, Adv. At. Mol. Phys. 18, 98 (1982).
[3]L. A. Lompre, G. Mainfray, C. Manus, S. Repoux, and J. Thebault, Phys. Rev. Lett. 36, 949 (1976).
[4]D. Normand and J. Morellec, J. Phys. B 13, 1551 (1980).
[5]M. Aymar and M. Crance, J. Phys. B 12, L667 (1979).
[6]L. A. Lompre, G. Mainfray, B. Mathieu, G. Watel, M. Aymar, and M. Crance, J. Phys. B 13, 1799 (1980).
[7]P. Agostini, F. Fabre, G. Mainfray, G. Petite, and N. K. Rahman, Phys. Rev. Lett. 42, 1127 (1979).
[8]P. Agostini, M. Clement, F. Fabre, and G. Petite, J. Phys. B 14, L491 (1981).
[9]P. Kruit, J. Kimman, and M. van der Wiel, J. Phys. B 14, L597 (1981).
[10]F. Fabre, G. Petite, P. Agostini, and M. Clement, J. Phys. B 15, 1353 (1982).
[11]P. Kruit, J. Kimman, K. G. Muller, and M. van der Wiel, Phys. Rev. A 28, 248 (1983).
[12]W. Zernik and R. W. Klopfenstein, J. Math. Phys. 6, 262 (1965); E. Karule, J. Phys. B 4, L67 (1971); 11, 441 (1978); S. Klarsfeld and A. Maquet, Phys. Lett. 73A, 100 (1979); J. Phys. B 12, L553 (1979); Phys. Lett. 78A, 40 (1980).
[13]Y. Gontier and M. Trahin, J. Phys. B 13, 4381 (1980).
[14]M. Aymar and M. Crance, J. Phys. B 12, L287 (1980).
[15]M. Aymar and M. Crance, J. Phys. B 14, 3585 (1981).
[16]S. Edelsteins, M. Lambropoulos, J. Duncanson, and R. S. Berry, Phys. Rev. A 9, 2459 (1974).
[17]G. Leuchs, S. J. Smith, E. E. Khawaja, and H. Walther, Opt. Commun. 31, 313 (1979).
[18]Y. Nagano, Y. Achiba, K. Sato, and K. Kimura, Chem. Phys. Lett. 93, 510 (1982).
[19]H. Kaminsky, J. Kessler, and K. J. Kollath, Phys. Rev. Lett. 45, 1161 (1980).
[20]F. Fabre, P. Agostini, G. Petite, and M. Clement, J. Phys. B 14, L677 (1981); R. Hippler, H.-J. Humpert, H. Schwier, S. Jetzke, and H. O. Lutz, J. Phys. B 16, L713 (1983).
[21]G. Leuchs and S. J. Smith, J. Phys. B 15, 1051 (1982).
[22]S. N. Dixit and P. Lambropoulos, Phys. Rev. Lett. 46, 1278 (1981).
[23]S. N. Dixit, J. Phys. B 16, 1205 (1983).
[24]M. Crance and M. Aymar, J. Phys. B 13, 4129 (1980).
[25]M. Crance and M. Aymar, J. Phys. B 13, L421 (1980).
[26]M. Aymar, M. Crance, and M. Klapisch, J. Phys. (Paris) 31, C4-141 (1970).
[27]M. Aymar and M. Crance, J. Phys. B 13, 2527 (1980).
[28]A. Dalgarno and J. T. Lewis, Proc. R. Soc. London, Ser. A 233, 70 (1955).
[29]M. Cervenan and N. Isenor, Can. J. Phys. 53, 1573 (1975).
[30]B. Cunin, J. A. Miehe, B. Sipp, M. Ya. Schelev, I. N. Serduchenko, and J. Thebault, Rev. Sci. Instrum. 51, 103 (1980).
[31]L. A. Lompre, G. Mainfray, and J. Thebault, Rev. Phys. Appl. 17, 21 (1982), and references therein.
[32]J. Morellec and D. Normand, J. Phys. B 14, 3919 (1981).
[33]P. Kruit and F. Read, J. Phys. E 16, 313 (1983).
[34]P. Kruit, thesis, University of Amsterdam (1982).
[35]A. l'Huillier, L. A. Lompre, G. Mainfray, and C. Manus, Phys. Rev. A 27, 2503 (1983).
[36]G. Breit and H. A. Bethe, Phys. Rev. 93, 888 (1954).
[37]E. Arnous, S. Klarsfeld, and S. Wane, Phys. Rev. A 7, 1559 (1973).